Journal of the Brazilian Society of Mechanical Sciences and Engineering (2026) 48:161
https://doi.org/10.1007/s40430-025-06138-z

TECHNICAL PAPER

# Effect of tool rotation speed on thermo-mechanical behavior in dissimilar FSW of 304L stainless steel and Ti–6Al–4V: a FEM-based approach

**Gulustan Tugce Alvali**[1,2] · **Yasin Sarikavak**[1]

Received: 26 June 2025 / Accepted: 4 November 2025
© The Author(s), under exclusive licence to The Brazilian Society of Mechanical Sciences and Engineering 2025

**Abstract**
Friction stir welding (FSW) is a solid-state welding method where mechanical and thermal changes are still not fully understood as a result of the complex nature of the phenomena involved. Theoretical simulation of the welding procedure performs a crucial function in predicting system behavior and optimization of the parameters and their levels. In this paper, an improved finite element model (FEM) was developed that considers time-dependent material properties and coupled thermal and mechanical analyses to investigate temperature and stress distribution during the process for dissimilar sheet metals of 304L stainless steel and Ti-6Al-4V alloy. The model incorporates various aspects such as the wear-resistant rotating tool, tool-workpiece geometry, temperature dependent material properties, travel, and tool rotation. The heat input in advancing and retreating side, frictional stress that leads the change in residual stress also investigated in detail. The model accurately simulates the processes at the tool-workpiece interface, where the developed model is validated with consistent accuracy compared to experimental results for the residual stress and temperature distribution parameters. The novelty of this work lies in addressing the limited literature on FSW of high-strength steel–titanium dissimilar pairs and in providing a validated thermo-mechanical FEM framework capable of capturing both temperature and residual stress under various rotational speed. A comparison of FSW trials revealed that the peak temperatures at 300 rpm and 350 rpm reach 977.35 °C and 1203.6 °C respectively. At 300 rpm 22.2 MPa stress difference observed from surface to depth of 1.59 mm (midpoint). However, for non-optimal FSW conditions sharp decrease and increase observed in the peak temperature and residual stress. In addition, the advancing side exhibited higher peak heat flux (~7 W/mm²) compared to the retreating side (~4 W/mm²), reflecting inherent process asymmetry. These findings provide the predictive capability of the proposed FEM framework for weld quality assessment.

**Keywords** Friction stir weld (FSW) · Dissimilar joint · Finite element method (FEM) · Temperature distribution · Stress state

## 1 Introduction

Friction Stir Welding (FSW) is a solid-state welding process established by The Welding Institute (TWI) in the United Kingdom at early 90s. The procedure includes a wear-resistant tool with rotation that generates friction and enables two materials to join below their melting temperatures in the solid phase. This solid-state welding results in a strong weld with excellent mechanical properties and minimal distortion [1, 2]. There are several independent variables in FSW, including tool rotation speed, travel, tool geometry, tilt geometry, and the force applied to analyze the contact at the tool and the workpiece materials. These parameters

Technical Editor: Lincoln Cardoso Brandao.

✉ Yasin Sarikavak
sarikavak@gmail.com

[1] Mechanical Engineering Department, Ankara Yıldırım Beyazıt University, 06010 Ankara, Türkiye

[2] Anova R&D Technologies Industry and Trade Inc. Co., 06510 Ankara, Türkiye

Published online: 02 February 2026

affect thermal distribution, mechanical properties of the weld, and residual stresses where these parameters have dominant effect on weld quality. Thus, simulating the welding procedure performs an essential function in predicting system behavior, mechanical strength and optimization of the process parameters.

Several studies have investigated the thermo-mechanical behavior of friction stir welding (FSW). Mohan and Wu (2021) reviewed FSW of steels and highlighted the challenges of joining high-strength alloys [1]. Dewangan et al. (2022) simulated heat distribution and stress in AA6082, confirming the critical role of rotational speed [3]. Sharma et al. (2022) performed experimental studies on aluminum alloys, reporting a reverse relationship between stress and tool speed [4]. Türkan and Karakaş (2022) modeled defect formation, emphasizing the importance of accurate thermo-mechanical representation [5]. Tunde Azeez and Mashinini (2022) used radiography to evaluate dissimilar aluminum welds, correlating weld integrity with processing parameters [6]. Shimpi et al. (2022) demonstrated the influence of tool pin profile on dissimilar joints using FEM [7]. Madhusudan et al. (2020) investigated transient thermo-mechanical response in dissimilar alloys [8]. Mugada and Adepu (2019) studied shoulder end features and their effect on weld quality [9]. Emamian et al. (2019) linked pin profiles and process parameters to weld strength in AL6061 [10]. Garg et al. (2019) analyzed progressive failure in AA6061–AA7075 joints using experiments and FEM [11]. Abbasi et al. (2015) provided a thermal analysis framework highlighting the effect of processing parameters [12].

Other recent studies further contributed to tool geometry optimization, defect modeling using CEL methods, and thermo-mechanical characterization of dissimilar joints [13–22]. While these works have advanced FSW understanding, few have addressed high-strength dissimilar pairs such as 304L stainless steel and Ti-6Al-4V, where both residual stresses and temperature evolution must be captured in a coupled framework.

Recent studies have expanded the scope of dissimilar FSW investigations. Gangwar and Ramulu (2024) reported residual stress measurements in dissimilar titanium alloy welds using X-ray diffraction, highlighting the importance of validating FEM predictions with advanced experimental techniques. They demonstrated that submerged FSW can effectively reduce thermal cycles and improve joint quality in dissimilar metal welding [23]. Wang et al. (2023) analyzed the influence of different FSW process variants on temperature evolution, residual stresses, and deformation. These contributions emphasize the continuing need for robust thermo-mechanical modeling of dissimilar joints [24]. In other studies, the Lagrangian approach has enabled the direct representation of advection terms and large deformations, while temperature and viscosity distributions in aluminum alloys have been obtained; however, the validation remains limited [25]. Tartakovsky et al. [26] introduces the SPH method for modeling material mixing and heat generation in FSW. Owing to its Lagrangian particle structure, free surfaces, void formation, and asymmetric temperature fields have been successfully captured; however, the material model was simplified and the experimental validation remained limited.

Quintana and Silveira (2018) experimentally investigated the effects of tool geometry (pin and shoulder) and process parameters (rotational, plunging, and traverse speeds) on the axial, longitudinal, and transverse forces in FSW of aluminum alloys, and reported that proper geometry–velocity combinations reduce overall forces and enhance process stability [27].

These approaches are computationally expensive and less suited for residual stress prediction. In contrast, the present FEM framework focuses on thermo-mechanical behavior and residual stress validation for 304L–Ti–6Al–4V dissimilar joints, to present a holistic approach to particle-based studies with a different perspective.

While numerous studies have modeled FSW of aluminum and copper alloys, far fewer investigations have addressed dissimilar high-strength combinations such as stainless steel and titanium alloys. Existing models often emphasize thermal histories or simplified material laws, but they rarely provide a coupled thermo-mechanical framework validated against both temperature and stress data. To address this gap, the present study develops an improved FEM for FSW of 304L stainless steel and Ti–6Al–4V. The novelty of this work lies in incorporating time- and temperature-dependent material properties, simultaneously predicting temperature fields and residual stress distributions, and validating the results against experimental benchmarks. This focused approach directly contributes to advancing the understanding of coupled thermo-mechanical behavior in dissimilar high-strength FSW joints.

In contrast to previous works that focused primarily on aluminum-based alloys or purely thermal analyses, this study uniquely contributes by: (i) extending coupled thermo-mechanical FEM to dissimilar high-strength alloys (i.e. 304L stainless steel and Ti-6Al-4V), (ii) integrating time- and temperature-dependent Johnson–Cook material properties to realistically capture strain-rate and thermal effects, and (iii) simultaneously predicting temperature fields and residual stress distributions validated against experimental data. These novelties ensure that the present work addresses key gaps in the literature and advances the scientific understanding of thermo-mechanical behavior in high strength dissimilar FSW.

**Table 1** 304L stainless steel temperature dependent material properties [28]

| Temperature (°C) | 0 | 200 | 400 | 600 | 800 | 1000 |
|---|---|---|---|---|---|---|
| Density (kg/m$^3$) | 7894 | 7744 | 7631 | 7518 | 7406 | 7406 |
| Thermal cond. (W/mºC) | 16 | 19 | 21 | 24 | 29 | 30 |
| Specific heat (J/kgºC) | 500 | 540 | 560 | 590 | 600 | 610 |

**Table 2** Ti-6Al-4V temperature dependent material properties [29]

| Temperature (°C) | 23 | 100 | 200 | 300 | 500 | 600 | 700 | 800 | 900 | 1000 |
|---|---|---|---|---|---|---|---|---|---|---|
| Thermal cond. (W/mºC) | 6 | 7.5 | 8.5 | 9.5 | 11.5 | 12.5 | 13.5 | 14.5 | 16 | 17.5 |
| Specific heat (MJ/kgºC) | 5.2e + 5 | 6.2e + 5 | 6.4e + 5 | 6.6e + 5 | 6.9e + 5 | 7.1e + 5 | 7.1e + 5 | 7.2e + 5 | 7.2e + 5 | 7.3e + 5 |

**Table 3** Johnson-Cook constitutive parameters [29]

| Material | A (MPa) | B (MPa) | *n* | C | m |
|---|---|---|---|---|---|
| 304L Stainless steel | 310 | 1000 | 0.65 | 0.07 | 1 |
| Ti-6Al-4V | 862 | 331 | 0.34 | 0.012 | 0.8 |

**Table 4** Main mechanical properties of Ti-6Al-4V and 304L stainless steel [35]

| | 304L Stainless steel | Ti-6Al-4V |
|---|---|---|
| Young's moduls (GPa) | 193 | 114 |
| Poisson's ratio | 0.3 | 0.34 |
| Coefficient of the thermal expansion (µmºC) | 18.7 | 87.9 |
| Yield stress (MPa) | 290 | 880 |
| Tangent moduls (GPa) | 2.8 | 0.8 |
| Density (kg/m3) | 4459 | 4430 |

**Table 5** Mechanical properties of employed PCBN tool [35]

| Young's moduls (GPa) | 680 |
|---|---|
| Poisson's ratio | 0.22 |
| Density (kg/m$^3$) | 4280 |
| Thermal cond. (W/mºC) | 100 |
| Specific heat (J/kgºC) | 750 |

## 2 Materials and methods

### 2.1 Material properties

In this study 304L stainless steel and Ti-6Al-4V plates with a thickness of 3.2 mm were used for FSW process of dissimilar materials. Tables 1 and 2 shows the employed temperature dependent properties of 304L stainless steel and Ti-6Al-4V. In FSW process, the friction coefficient varies as an uncertain variable due to the violent nature of the process and the combination of friction and heat generated by the rotating tool and advancing motion is utilized to join the materials.

Various tool rotation speeds of 150 rpm, 200 rpm, 300 rpm, 350 rpm and 450 rpm were used to elaborate the effect of tool rotation on the thermal and mechanical properties of dissimilar joint by using a PCBN tool with a shoulder diameter of 18.5 mm and the pin diameter of 12.64 mm. The developed model was validated using experimental data [28] for temperature and stress values reported in the literature.

The material behavior was assumed isotropic in the elastic–plastic regime, which is a common simplification in FSW simulations. In the present study, the workpieces were dissimilar 304L stainless steel and Ti–6Al–4V. Temperature dependent material parameters correspond to these alloys and are reported in Tables 1 and 2, while the Johnson–Cook viscoplastic parameters are listed in Table 3 [28–30].

The material properties for engineering data of finite element simulation requires both thermo-physical properties including heat capacity, thermal conductivity density; and thermo-mechanical properties such as Poisson's ratio, modulus of elasticity, thermal expansion coefficients, tensile and yield properties [31, 32]. To achieve accurate simulation results, it is crucial that these material properties be defined as temperature-dependent functions across the entire temperature range, spanning from room temperature to elevated temperatures encountered during the process. Thus, the temperature dependent material properties defined in the model. Main mechanical properties of dissimilar workpiece materials can be seen in Table 4 [33, 34]. The tool and the pin materials are made of PCBN and the basic material properties of PCNB are given in Table 5 [35, 36].

Mechanical properties in Table 4 were taken as nominal (temperature-independent) values to simplify the model and reduce computational cost, in line with similar FSW simulations [28, 30]. The density of Ti–6Al–4V was assumed constant, as its variation over the studied temperature range is negligible.

The thermophysical properties of 304L stainless steel and Ti–6Al–4V were obtained from different literature sources, due to the absence of a single comprehensive dataset for both alloys across the relevant temperature range. To ensure consistency, the datasets were cross-checked for overlapping temperature ranges and smooth variation of density, thermal conductivity, and specific heat. Normalization

against established handbook values confirmed that merging these sources provides a coherent and physically realistic property database for the simulations. This approach ensures that, although derived from different references, the material data used in the model remain reliable and consistent for predicting thermal and mechanical responses during FSW.

## 2.2 Methodology

A 3-D model was developed to demonstrate the thermal and mechanical gradients throughout the thickness where the simulation was performed in three steps i.e. immersion, mixing and travel. The rotation and gradual travel of the tool on the sheet metals as workpiece were taken into account to obtain the stress distribution and temperature during the process.

### 2.2.1 Theoretical background

FSW requires multiple physical phenomena, where the material flow exhibits a relation on thermal and mechanical properties. The validity of simulation is intrinsically linked to the accurate representation and the implementation of a suitable constitutive model such as the Johnson-Cook (JC) model considers the material's mechanical and thermal properties simultaneously. The JC model is a visco-plastic model that accounts for both strain rate and temperature dependencies, is particularly well-suited for simulating high strain rate processes like FSW. The used JC model is given in Eq. 1 [20, 37].

$$\sigma = [A + B.\epsilon^{n}]\left[1 + C.\left(\frac{\dot{\epsilon}}{\dot{\epsilon}_{0}}\right)\right]\left[1 - \left(\frac{T - T_{room}}{T_{melt} - T_{room}}\right)^{m}\right] \quad (1)$$

Here, σ is the shear stress, A is the initial yield strength of the material (MPa), ε is the effective strain, $\dot{\epsilon}$ is the strain rate, $\dot{\epsilon}_{0}$ is the reference strain rate (1.0 $s^{-1}$), $T_{room}$ is the room temperature (°C), and $T_{melt}$ is the melting temperature (°C) of the material. Here, B is the hardening modulus (MPa), C, m and n are the strain rate sensitivity coefficient, thermal softening coefficient, and strain hardening coefficient respectively.

At the tool and workpiece interface shear stress generated and the formula for the shear flow stress of workpiece according to Von-Mises criteria is given in Eq. 2 [1, 3].

$$\tau_{yield} = \frac{\sigma_{yield}}{\sqrt{3}} \quad (2)$$

In accordance with the Coulomb friction law, the shear stress is determined by Eq. 3. In this equation, P represents the normal pressure exerted at the interface between the tool and the workpiece, while μ denotes the friction coefficient. When operating at low angular velocities, this equation shows valid results for simulating the FSW process [8, 38].

$$\tau_{f} = \mu .P \quad (3)$$

At the interface according to the plastic deformation and friction, heat generation ( $q_p$) in can be defined as follows [5].

$$q_p = n.\tau .\dot{\epsilon}_{pl} \quad (4)$$

In Eq. 4, η is a coefficient according to change in plastic energy to temperature, which is used as 0.3. Shear stress is represented with $\tau$ and $\dot{\epsilon}_{pl}$ is the plastic strain rate [19, 39, 40].

In this study, η was taken as 0.3, consistent with the widely accepted Taylor–Quinney coefficient range (0.2–0.5) reported in the literature. This value assumes that approximately one-third of the plastic work is dissipated as heat, while the remaining energy is stored in microstructural defects and phase transformations. The selection of η = 0.3 provides stable numerical results and yields good agreement with experimental data [41].

The heat generated by friction between the tool and the workpiece ( $q_f$) is calculated by Eq. 5, which is the shear stress caused by friction, $\dot{\gamma}$ is the traverse speed [42].

$$q_f = \tau_{f}.\dot{\gamma} \quad (5)$$

The heat input (q) during FSW is calculated by the Frigaard equation independent of tool feed rate [17].

$$q = \int_{0}^{R} 2.\pi .\mu .\omega .P.r^{2}.d.r \quad (6)$$

In Eq. 6, tool shoulder radius represented with *R*, radius of the tool pin is *r*, where $\mu$ represents friction coefficient, and *P* and $\omega$ are the pressure, and angular velocity respectively.

Considering only shoulder frictional heating (Eq. 6) would be incomplete. In the present model, heat from plastic deformation beneath the pin is also included through Eq. (4) with η = 0.3 in the Johnson–Cook law. Thus, both heat sources—shoulder friction and pin-induced plastic deformation—are represented, ensuring a realistic thermo-mechanical description consistent with experimental validation [41].

Heat transfer observed in actual case where three-dimensional transient heat conduction exist according to Fourier's

equation. Equation 7 shows the conduction heat transfer equation used in the model [43, 44].

$$\rho .c.\frac{\partial (T)}{\partial t} = \frac{\partial}{\partial x}.\left(k_x.\frac{\partial T}{\partial x}\right) + \frac{\partial}{\partial y}.\left(k_y.\frac{\partial T}{\partial y}\right) + \frac{\partial}{\partial z}.\left(k_z.\frac{\partial T}{\partial z}\right) \tag{7}$$

In this model, $c$ represents heat capacity, $T$ represents temperature, $\rho$ represents density, and $kx$, $ky$, $kz$ represent thermal conductivities changes with temperature along their respective coordinate axes. However, the aluminum workpiece is assumed to be an isotropic material, meaning its thermal conductivity is uniform in all directions. Consequently, a single thermal conductivity value, denoted as k, will be used for all three perpendicular directions (kx = ky = kz = k).

Coordinate system moves with a velocity of $Vx$ (source velocity) along the positive x-axis on the workpiece. The heat transfer equation for the workpiecematerial can be seen in Eq. 8 [44].

$$\rho .c.\left(\frac{\partial T}{\partial t} + v_x.\frac{\partial T}{\partial x}\right) = \frac{\partial}{\partial x}.\left(k_x.\frac{\partial T}{\partial x}\right) + \frac{\partial}{\partial y}.\left(k_y.\frac{\partial T}{\partial y}\right) + \frac{\partial}{\partial z}.\left(k_z.\frac{\partial T}{\partial z}\right) \tag{8}$$

$$\tau = -P.g.(\Delta v_g).\frac{\Delta v_g}{|\Delta v_g|} \tag{9}$$

Equation 9 defines $\tau$ as the shear stress where $P$ is pressure, and $g(\Delta v_g)$ is the relative sliding velocity between the traverse speed and material speed [2].

The validated model employs a code named WELDSIM that utilizes Fourier's heat equations to simulate heat transfer [28].

$$\rho .c_p.\frac{\partial T}{\partial t} = \nabla .(k.\nabla T) + Q \tag{10}$$

In Eq. 10, $k$ thermal conductivity, and $Q$ Internal heat generation [44].

These governing equations collectively define the thermo-mechanical framework employed in this study, ensuring that both frictional and plastic deformation heat sources are represented together with transient heat conduction.

The above set of equations forms the governing framework for the finite element formulation, combining heat conduction, plastic deformation, and frictional heat generation. These equations are directly implemented into the FEM solver to describe the coupled thermo-mechanical response during FSW.

### 2.2.2 Meshing and boundary conditions

The combined thermal and mechanical models were used for FEM. The deformable solid plates made of 304L stainless steel and Ti-6Al-4V have dimensions of 76.2 × 60 × 3.2 mm³ used as workpiece materials. The employed tool shoulder diameter and the pin diameter is 18.5 mm, and 12.64 mm respectively. The HEX20 elements are used for the mesh in the FEM model both for workpieces and the tool. For the sections where there is interaction between tool shoulder and workpiece fine mesh used for the accuracy in the violent thermo-mechanical process and for the rest of the sections relatively coarse elements employed for the meshing process. In the FEM, the plates consisted of 55,805 nodes, and 9988 elements (20-node hexahedral (HEX20) elements). The meshed model and the employed boundary conditions can be seen in Fig. 1. A refined mesh was applied around the tool–workpiece interface to capture steep gradients in stress and temperature. The transient analysis was solved using automatic time stepping, which allowed stable and accurate convergence of the coupled thermo-mechanical fields. The simulation was conducted in three sequential stages: (i) tool plunging, (ii) rotation to induce material flow, and (iii) a combined rotation and traverse stage.

In FSW, at the top and side surfaces a convective heat transfer coefficient of 30 W/m2ºC was defined for natural convection among the plates and the air. A convective coefficient of 350 W/m2ºC is implemented to the bottom surface of the workpiece as a boundary condition. The edges of the

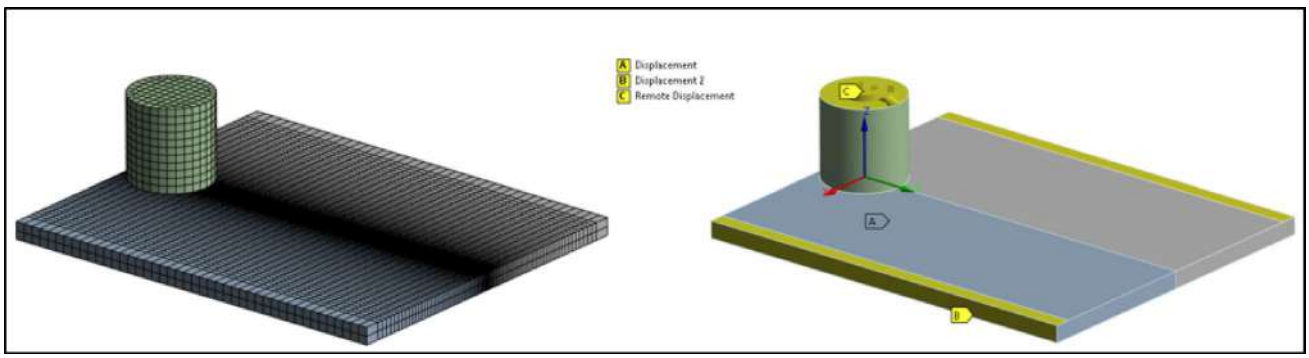


**Fig. 1** The schematic representation of the meshed FSW process

workpiece were fixed, in the initial stage of the analysis, in a way that prevents bending of the surface in -x, -y, -z and rotational directions (see Fig. 2). The tool was represented as a rigid body without thermal degrees of freedom in the model.

The convective heat transfer coefficients were defined as 30 W/m²·°C at the top surface and 350 W/m²·°C at the bottom surface, consistent with previous FSW thermal analyses [28, 45]. The smaller value corresponds to natural convection with the ambient air, whereas the higher value represents effective heat removal through the backing plate, modeled as an equivalent convective sink. No external forced convection was applied. Radiation heat transfer to the environment was neglected, since its contribution (< 5%) is insignificant compared to conduction and convection in FSW, consistent with previous studies [28, 44, 46]. A low thermal contact conductance (10 W/m²·°C) was defined between the tool and the workpiece, with 95% of the generated heat flux partitioned into the workpiece and 5% into the tool, following established modeling practice [46]. Although the PCBN tool conductivity was included in the material definition, its effect remained secondary due to this partitioning approach.

Boundary conditions are illustrated: the bottom surface is fixed in all translational DOFs, lateral faces prevent rigid motion but allow free longitudinal expansion, and remote displacement is applied axially to simulate the forging force. Thermal boundary conditions include convection (30 W/m²·°C top, 350 W/m²·°C bottom) and adiabatic symmetry planes (Figs. 1 and 2).

The detailed mesh, boundary conditions, and heat transfer definitions are provided to ensure reproducibility and clarity of the numerical procedure. The bottom surface of the plate was fully constrained in translational DOFs, while the lateral faces were restricted to avoid rigid body motion but allowed to expand in the welding direction. The remote displacement condition was applied in the vertical direction to replicate the axial forging load. For the thermal analysis, natural convection was applied at the top surface, an effective convective sink was imposed at the bottom surface, and symmetry planes were treated as adiabatic.

## 2.3 Model validation

The experimental dataset of Zhu anf Chao [28] was selected for validation because it provides one of the few published results including both temperature evolution and residual stress measurements for FSW. The geometry of the specimens, tool configuration, and measurement methodology are consistent with the simulation setup, ensuring reliable comparison.

The obtained stresses and temperature values were determined for a travel of 101.4 mm/min and 300 rpm by considering the experimental study. The validation was made between the temperatures obtained from the developed model and the experimental work conducted by Zhu and Choa [28] (Fig. 3). The numerical results for joined 304L stainless steel indicate that the highest temperature was seen below the shoulder at center point and gradually decreasing from the center of the plates towards the edges. The experimentally obtained temperature is 550 °C, 15.3 mm apart from the weld line while FEM result calculated as 580 °C at the same point. Similarly experimental temperature via thermocouple 20.64 mm apart from the weld line is 153.8 °C while FEM result shows 160 °C at the same point. These data show the model validated with acceptable accuracy for the thermal distribution.

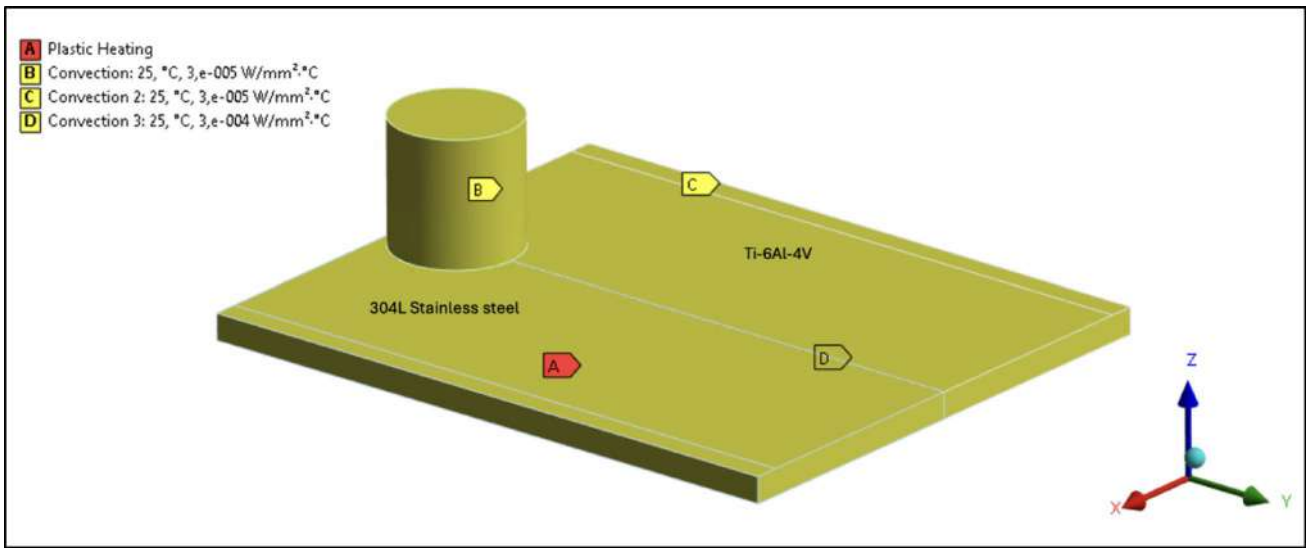


**Fig. 2** Dissimilar joints and thermal boundary conditions

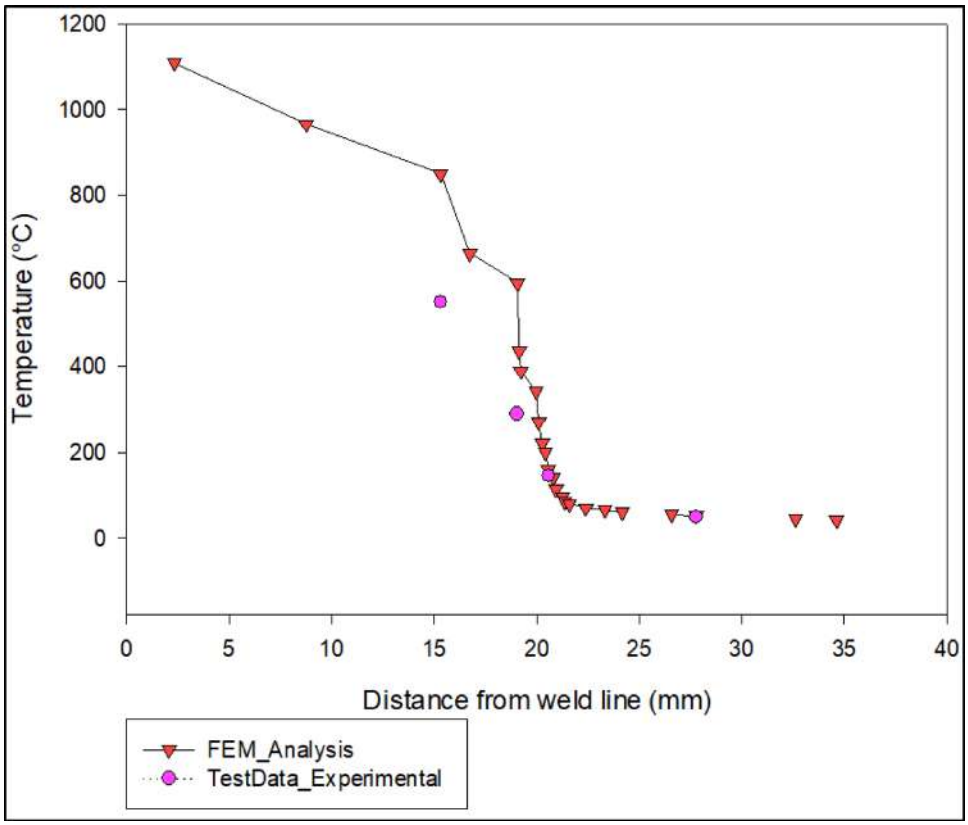


**Fig. 3** Experimental [28] and theoretical temperature distribution from weld line

In addition to temperature, a comparison of residual stresses was also conducted with the study of Zhu and Chao [28]. In Fig. 4 the highest residual stress obtained at the center point of the weld line with 473 MPa while experimental results reported this value as 376 MPa. The experimental and FEM results 4.72 mm apart from the weld line below 1.3 mm to the workpiece surface investigated as 364 MPa for both results with high accuracy.

As a result, thermal and mechanical FEM for temperature and residual stress parameters are validated with adequate consistency. According to the validated thermal and mechanical results the developed model gives realistic results when compared with the actual process.

For dissimilar joint simulations investigated heat flux ($W/mm^2$) values for the validated model during the process are given in Fig. 5 [47, 48]. The process strongly dependent to the process parameters. When the tool rotational direction and travel are in the same direction this is called advancing side (AS) and when tool rotational direction is opposite with travel direction defined as retreating side (RS). Many studies in the literature reported that AS generates additional heat due to friction and heat transfer when compared with RS [33, 34]. Figure 5 clearly shows that the analyzed heat flux in advancing side reaches above 7 W/mm2 where at the same position in retreating side this value decreased below 4 W/mm2. Apart from the tool diameter the applied heat flux sharply decreases to zero with a distance from weld line. The results show that the developed model highly sensitive and accurate to analyze the difference in both AS and RS.

The Advancing Side (negative distance) exhibits a higher peak heat flux (~7 $W/mm^2$) due to stronger frictional and plastic deformation, while the Retreating Side (positive distance) shows a lower peak (~4 $W/mm^2$) with smoother decay. This asymmetry reflects the inherent difference between AS and RS in FSW for dissimilar high strength joints.

The validation results confirmed that the assumption of $\eta = 0.3$, within the commonly reported Taylor–Quinney coefficient range, ensures consistency between simulated and experimental temperature distributions and residual stresses.

Unlike Al–steel FSW studies, where the tool is typically offset toward the softer aluminum side to enhance mixing and reduce defects [49], the present dissimilar pair of 304L stainless steel and Ti–6Al–4V exhibits less severe hardness mismatch. Preliminary simulations with offset values led to strong mesh distortion without notable benefits in temperature distribution. Therefore, the tool was positioned along the weld centerline to ensure numerical stability and reliable model validation.

The validation in this study primarily relied on a single published dataset due to the limited availability of measurements for 304L and Ti–6Al–4V joints. While this is a

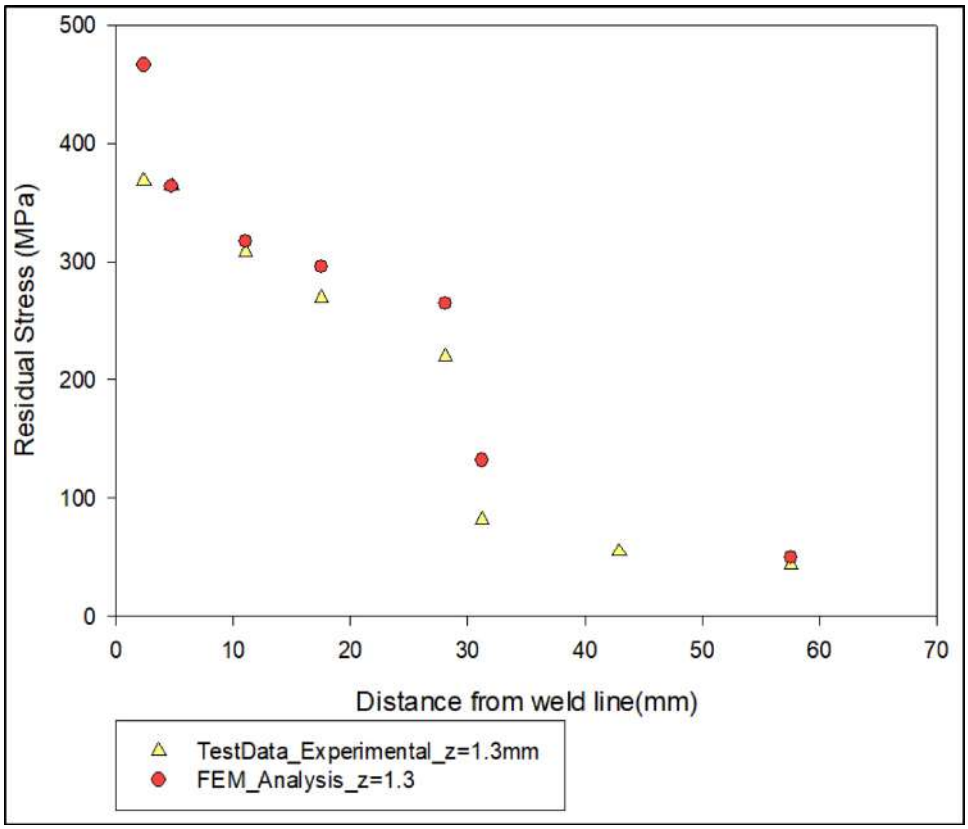


**Fig. 4** Experimental [28] and theoretical residual stress distribution

limitation, the results were cross-checked across multiple points within that dataset and were consistent with trends reported in other high-strength alloy FSW simulations [30, 45].

Some discrepancies between the model and experiments were observed, particularly in peak temperature and residual stress values at the weld center. These can be attributed to simplifications in boundary conditions, uncertainties in material data, and experimental measurement limitations. Solid state welding of dissimilar high strength materials results with instability and chatter during the actual process that causes uncertainties for experimental data collection. Nevertheless, the overall agreement with experimental trends confirms the validity of the model.

It should be noted that the validation in this study is primarily based on the data of Zhu and Chao (2004), as this remains one of the few experimental datasets providing both temperature and residual stress for FSW of high strength sheets. Nevertheless, the trends predicted by the model are consistent with other works [38, 45], showing additional confidence to the results.

## 3 Results and discussion

Unlike WELDSIM, which is limited to Fourier-based thermal simulations, and CEL/ALE formulations, which suffer from high computational cost and stability issues, the present work provides a coupled thermo-mechanical FEM framework using the Johnson–Cook law with time- and temperature-dependent material properties. This enables simultaneous prediction of thermal and stress fields in high-strength dissimilar joints, which has not been adequately addressed in previous models.

Both literature and preliminary simulations indicate that tool rotational speed exerts the most significant effect on heat generation and thermal response, followed by traverse speed, with tilt angle and axial force having comparatively smaller influence within the studied range [38, 45].

### 3.1 Effect of rotational speed in FSW

Effect of changes in the joining parameters of FSW cause variations in the post-weld mechanical and thermal properties. This section explores the process parameters on mechanical and thermal properties of welded joints in FSW that in the developed model the tool rotational speed was varied (150 rpm, 200 rpm, 300 rpm, 350 rpm, and 450 rpm) where travel kept constant with 360 mm/min with a tool

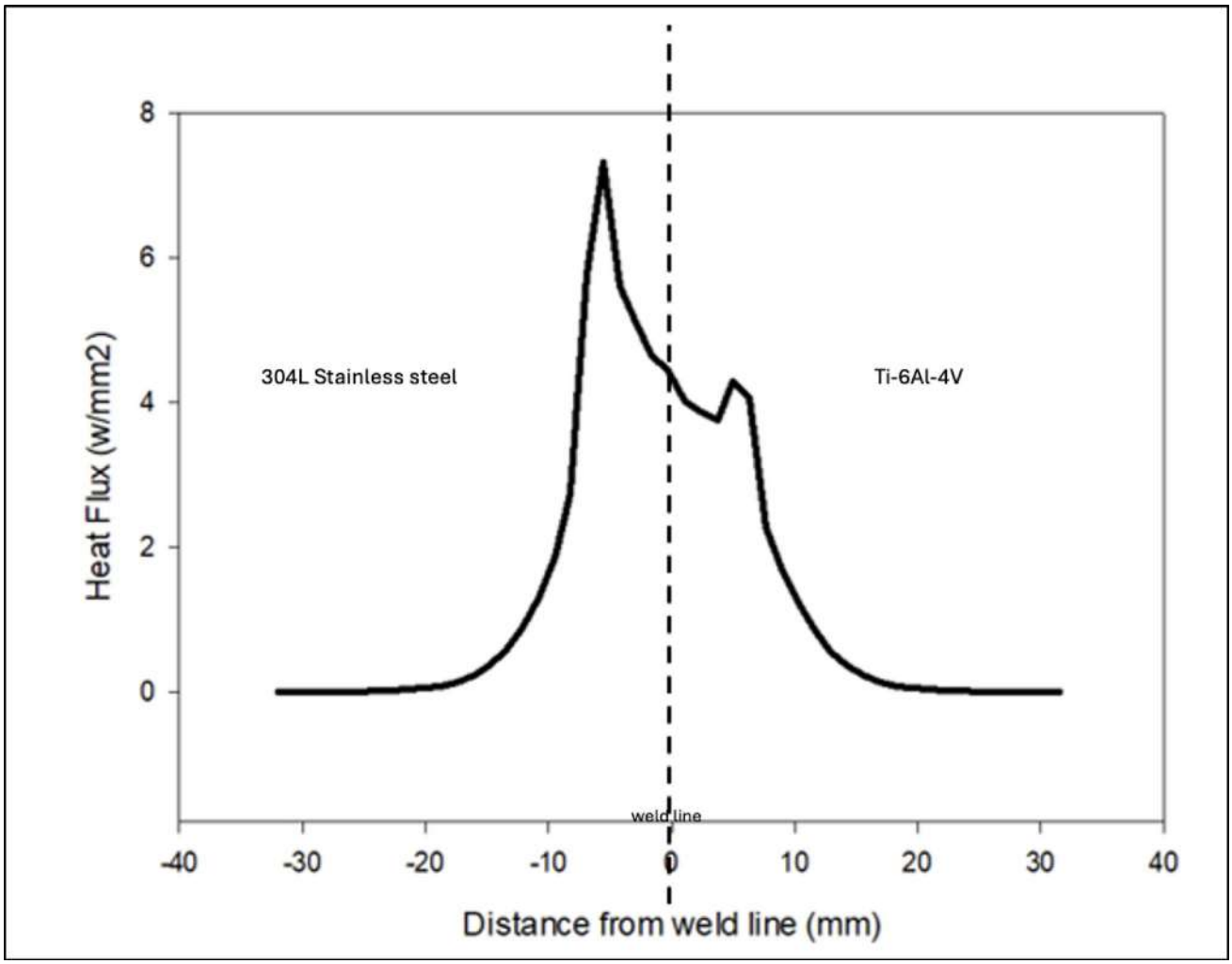


**Fig. 5** Heat flux values for advancing and retreating side in workpiece

radius of 7.62 mm. Thus, the effect of rotational speed on the FSW process was investigated for dissimilar joints.

The provided information indicates that the welding of Ti6Al4V and 304L stainless steel plates was performed in a single pass. Temperature and stress values were collected during the FSW process at specific locations at the bottom and top surfaces and at the middle of the plate. Stress values have been obtained at depths of 0.795 mm, 1.59 mm, 2.385 mm, and from the plate surface with a path through z axis (see Fig. 6).

Figure 7 shows the temperature distribution through the process time where for the lower rotational speeds relatively less difference observed in the temperature change however for the higher rotational speeds wide range of thermal difference observed on the workpiece surface during the process period. The maximum temperature value was found to be 136.18 °C at 150 rpm. The increase in tool rotation speed resulted with sharp rise in the peak temperature where 284.25 °C, 977.35 °C, 1203.6 °C, and 1787.3 °C were obtained under 200 rpm, 300 rpm, 350 rpm, and 450 rpm respectively. To clarify the temperature distribution in the dissimilar joint, the Fig. 7 shows the maximum temperature and its distance from the weld line during the process. The maximum temperatures observed at tool workpiece interface for the locations adjacent to weld line on the stainless-steel side of the joint. The gradual decrease in temperature observed for both sections when getting closer to the plate's edges (see Fig. 7).

Figure 7 illustrates the temperature distributions at different depths for 300 rpm and 350 rpm. At 300 rpm, the maximum temperature was measured as 977.35 °C, whereas at 350 rpm it reached 1203.6 °C. Thus, an increase in tool rotation speed resulted in approximately a 23% rise in the peak temperature.

Residual stress is crucial for understanding the weld quality of the joint. The obtained residual stresses at the workpiece surface, and depths of 0.795 mm, 1.59 mm (middle of plates) and 2.385 mm are evaluated in Fig. 9.

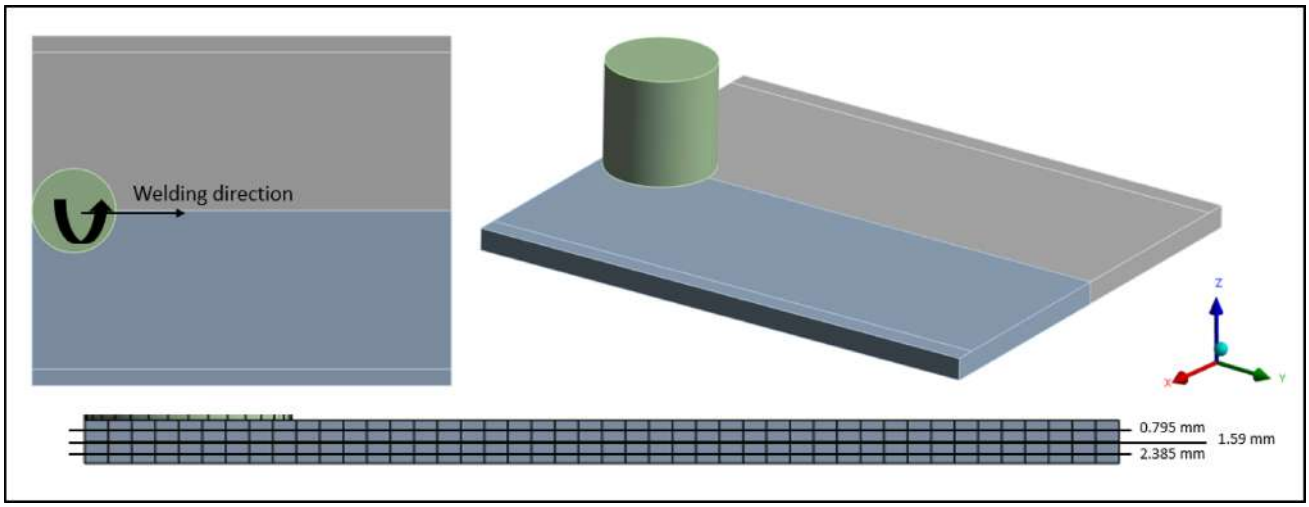


**Fig. 6** Location of collected data for stress and temperature in FSW

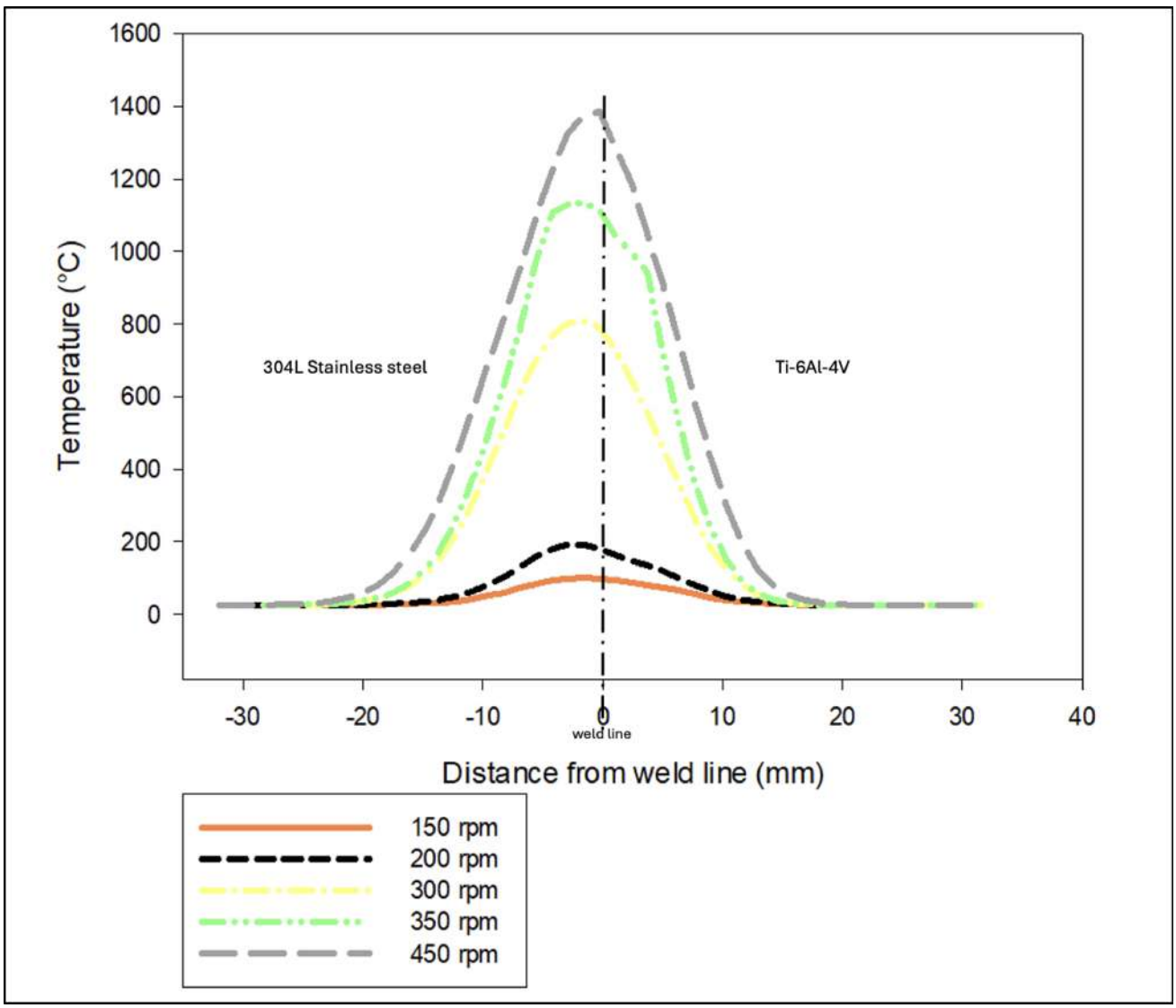


**Fig. 7** Temperature values thorough weld line for the dissimilar joint

The increase in tool rotation speed resulted with increase in the residual stress at surface of plates where 30.212 MPa, 63.522 MPa, 470.76 MPa, 554.6 MPa, and 983.56 MPa were obtained under 150 rpm, 200 rpm, 300 rpm, 350 rpm, and 450 rpm, respectively. The residual stress values at 150 rpm were 30.405 MPa, 30.617 MPa and 29.552 MPa at 0.795 mm, 1.59 mm, and 2.385 mm depth respectively. Similarly at 200 rpm investigated values are 63.929 MPa, 64.4 MPa and 62.203 MPa at 0.795 mm, 1.59 mm and 2.385 mm depth respectively. For 300 rpm, 350 rpm and 450 rpm rotational speeds 430.84 MPa, 422.52 MPa and 412.6 MPa; 522.64 MPa, 509.32 MPa and 499.64 MPa; 744.87 MPa, 566.7 MPa and 524.25 MPa residual stresses obtained for the locations at a depth of 0.795 mm, 1.59 mm, and 2.385 mm respectively (Fig. 8).

For the 150 rpm and 200 rpm rotational speeds, obtained residual stresses are lower however for the 300 rpm, 350 rpm and 450 rpm tool rotational speeds, a dramatic rise investigated in terms of residual stresses for the dissimilar joint. At suboptimal parameters, such as 450 rpm, a marked increase in residual stress is observed, which can compromise joint integrity by inducing defects such as distortion and discontinuities.

Figure 9 presents the residual stresses generated at different depths for 300 rpm (a) and 350 rpm (b). At 300 rpm, the maximum residual stress at the surface was measured as 430.84 MPa, whereas at a depth of 1.59 mm it decreased to

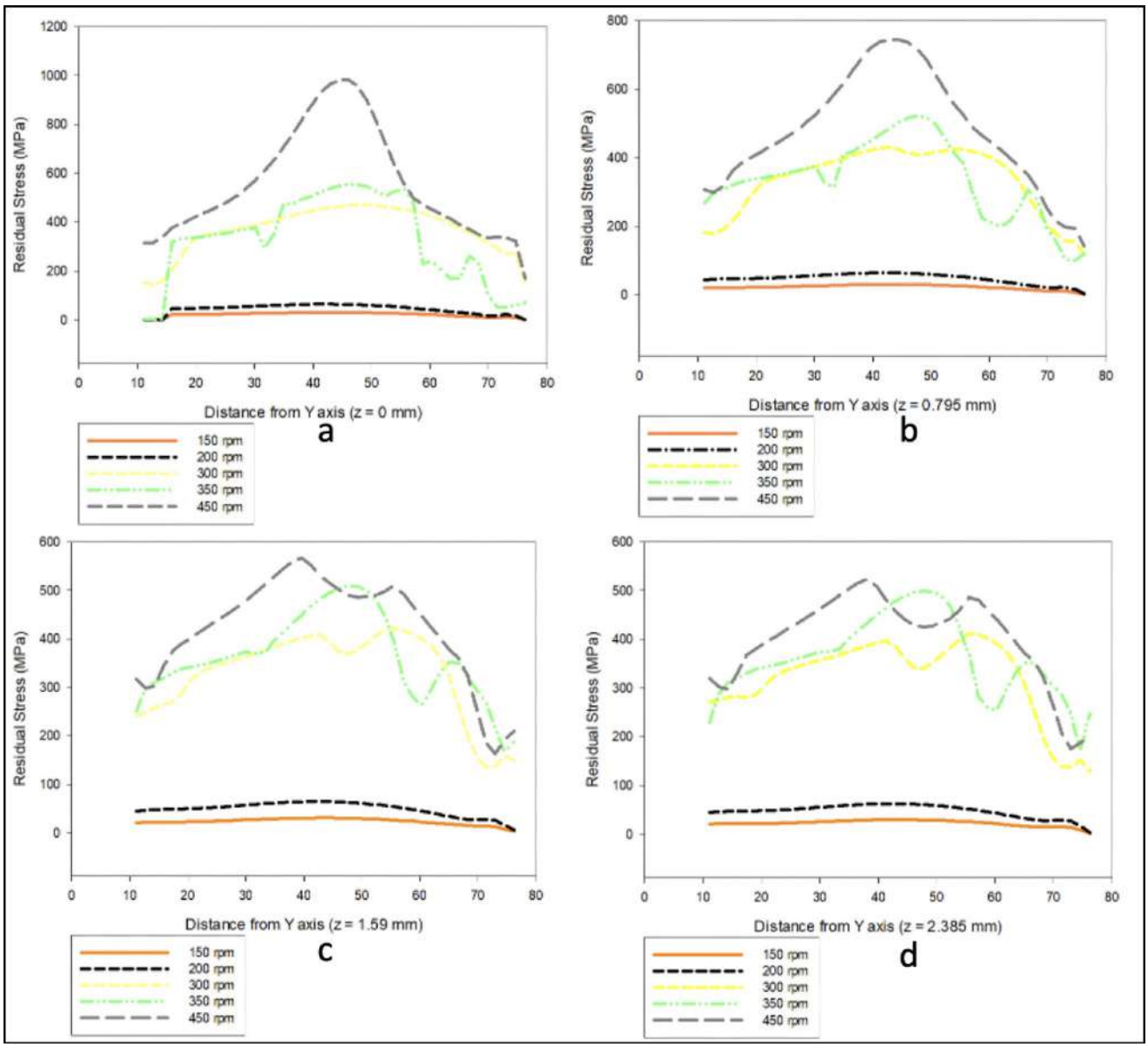


**Fig. 8** Residual stress values at a depth of **a** 0 mm **b** 0.795 mm **c** 1.59 mm and **d** 2.385 mm

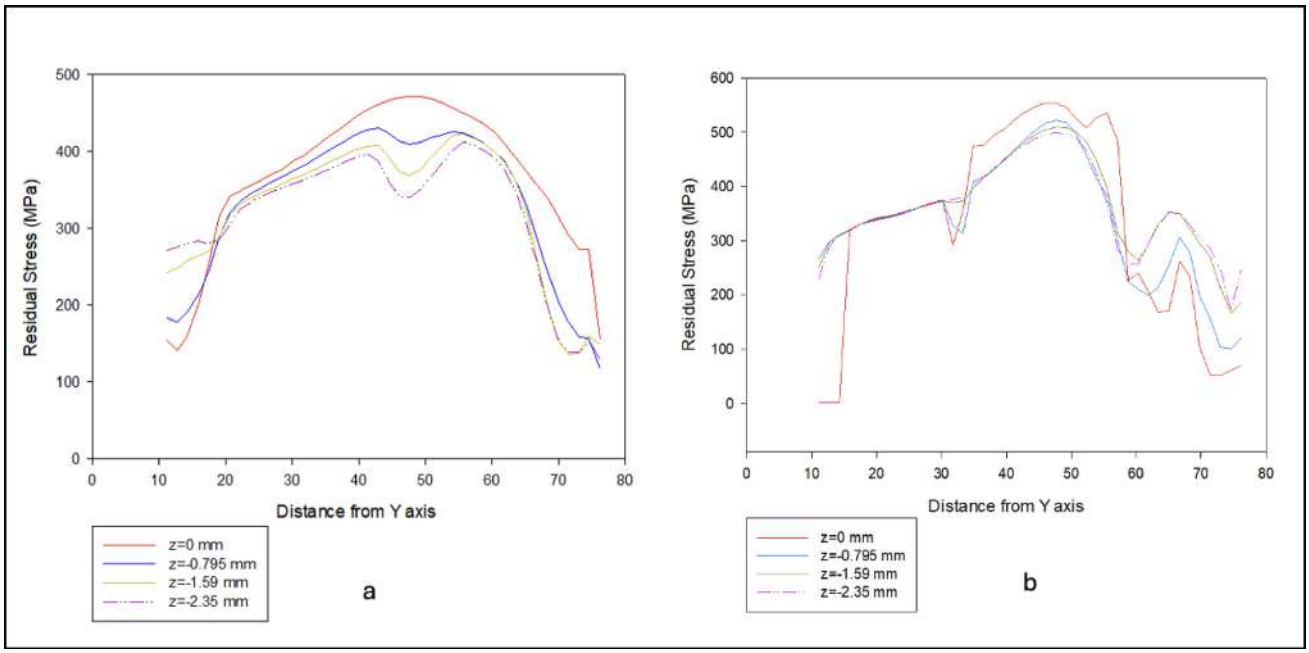


**Fig. 9** Residual stresses values at different depth of **a** 300 rpm **b** 350 rpm

408.6 MPa. Similarly, at 350 rpm, the residual stress measured at the surface was 522.64 MPa, whereas at 1.59 mm it was 509.32 MPa. These results indicate that the higher residual stress observed at the surface area where tool and sheet interact and this gradually decreases through the thickness.

Since heat input and thermal change is one of the major factors for weld quality, the effect of rotation speed was investigated by means of heat flow values occurring in the FSW process. The heat flux approached almost zero at the tool centre location and gradually increases towards the midpoints of the plates (Fig. 10).

The maximum heat flux values have calculated at (61.48 mm from Y axis) as 0.028 W/m$^2$ at 150 rpm, 0.057 W/m$^2$ at 200 rpm, 0.56453 W/m$^2$ at 300 rpm, 0.67211 W/m$^2$ at 350 rpm and 0.86983 W/m$^2$ at 450 rpm for the advancing side; 0.012 W/m$^2$ at 150 rpm, 0.026 W/m$^2$ at 200 rpm, 0.30498 W/m$^2$ at 300 rpm, 0.36883 W/m$^2$ at 350 rpm and 0.49822 W/m$^2$ at 450 rpm for the retreating side.

The heat flow distribution around the contact surface is unsymmetrical with respect to the weld centerline, as seen in Fig. 10.

As presented in Fig. 10, the AS consistently shows higher peaks whereas the RS shows lower but broader gradients, in line with typical FSW asymmetry.

Figures 5 and 10 together illustrate the strong coupling between thermal fields and residual stresses in the present FSW model. The temperature distribution in Fig. 5 reveals a clear asymmetry between the advancing side (AS) and the retreating side (RS), with higher peak temperatures observed on the AS due to the additive effect of tool rotation and traverse motion. This asymmetric heating has important consequences for weld integrity, as it promotes grain coarsening and local softening on the AS. The residual stress map shown in Fig. 10 further reflects this behavior, with tensile stresses concentrated at the weld centerline and compressive stresses in the adjacent regions. Such a stress pattern arises from steep thermal gradients during cooling and agrees with experimental observations in dissimilar FSW joints [28]. The correspondence between Figs. 5 and 10 thus confirms that the non-uniform temperature distribution directly contributes to the residual stress state, providing insight into potential defect-prone regions and highlighting the predictive capability of the present thermo-mechanical framework.

The theoretical background of this asymmetry can be attributed to the coupled effect of tool rotation and traverse motion. On the Advancing Side, the local strain rate and sliding velocity are higher, leading to enhanced frictional dissipation and plastic work, which explains the higher heat flux observed in Figs. 5 and 10. In contrast, the Retreating Side experiences lower relative velocity and reduced plastic deformation, resulting in smoother but lower heat flux distributions. This imbalance in heat generation directly contributes to the development of tensile residual stresses along the weld centerline and compressive zones adjacent to it, consistent with the predictions of the Johnson–Cook viscoplastic model adopted in this study. Thus, the thermo-mechanical asymmetry is not only observed numerically

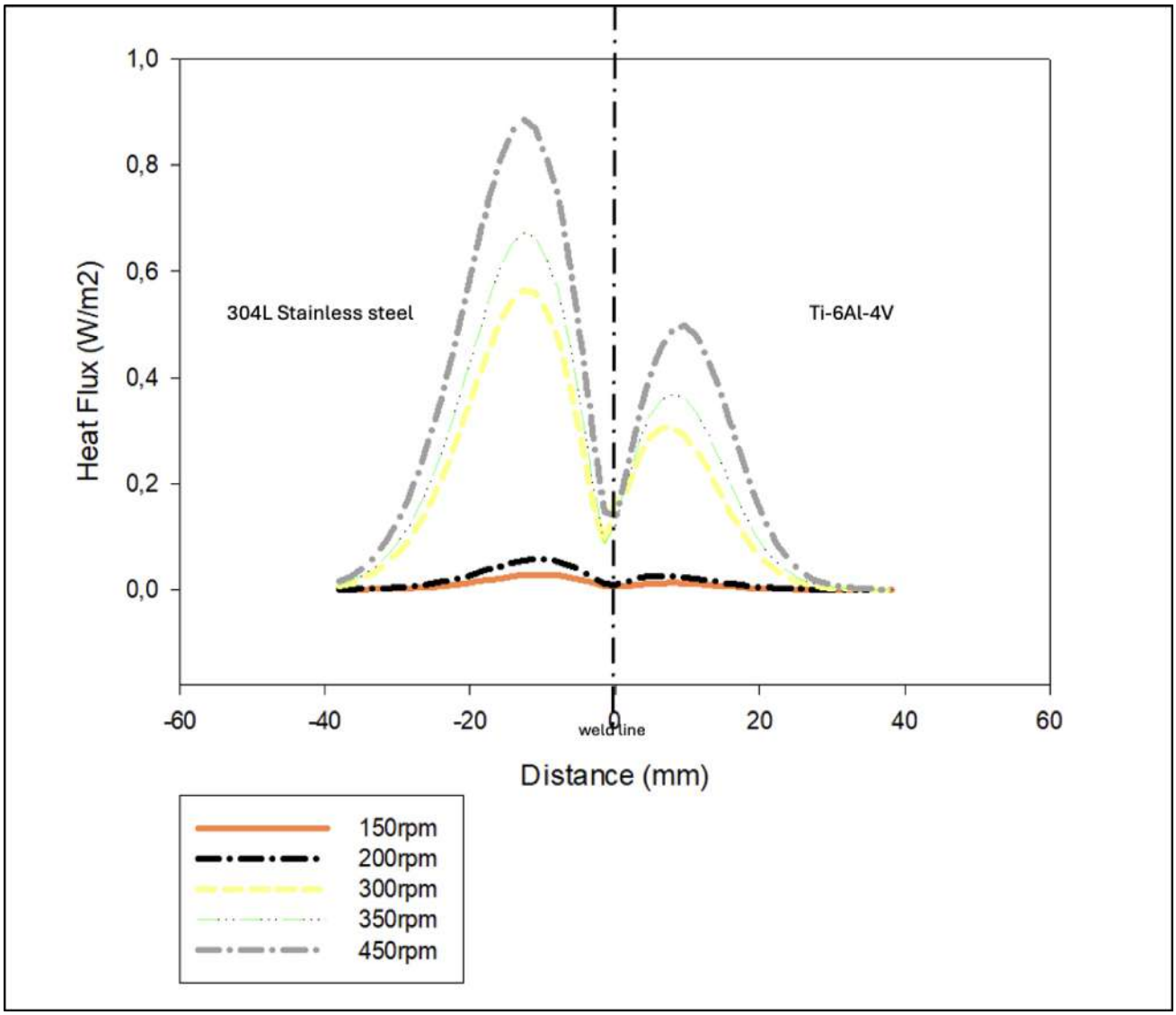


**Fig. 10** Heat flux values

but also theoretically supported by the governing physical mechanisms.

Friction stress has a direct impact on both heat generation and microstructure formation in FSW thus this parameter examined in Fig. 11. The plastic deformation caused by friction stress refines the grain structure and influences the phase transformations. Friction stress also performs a position in the formation of residual stresses in the weld zone. Figure 11 demonstrates that as the tool rotation speed increases, so does the friction stress. A sudden rise experienced at the 7.5th second in friction stress upon the tool's contact with the plate.

The asymmetric thermal fields observed in the simulations explain the tensile residual stresses concentrated along the weld centerline and the compressive stresses toward the sides. This behavior is consistent with previously reported trends in dissimilar FSW [38, 45]. Although direct experimental tests for 304L–Ti–6Al–4V joints were not performed within this work, validation against the experimental results of Zhu & Chao (2004), together with consistency across other studies, supports the reliability of the model. Future work will extend the verification by incorporating dedicated experiments on this specific material system, thereby enhancing the predictive capability of the proposed framework.

## 4 Conclusion

In this study, a 3-D FEA based model was developed to simulate the process for dissimilar joints. The validated model offers a suitable framework for conducting realistic analyses

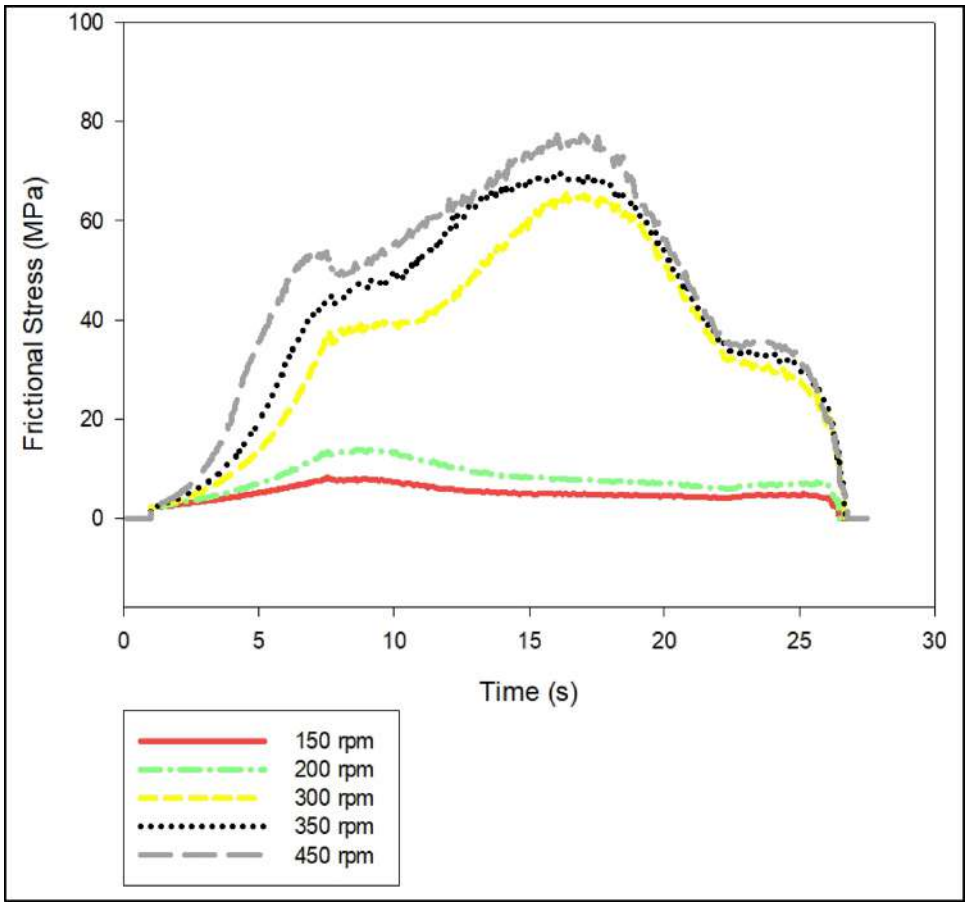


**Fig. 11** Frictional stress values thorough process time

of time dependent mechanical stress, temperature distribution and detecting defect formation in FSW. The accuracy of numerical simulations in FSW heavily relies on the precise determination of the boundary conditions, which is influenced by the complex nature of the process.

This research focuses on FSW to join two high strength dissimilar materials, that are difficult to weld by conventional methods such as 304L stainless steel and Ti6Al4V plates by using a PCBN tool. The model was simulated at four distinct tool rotation speeds, and the resulting temperature and the stress distributions were investigated.

Rotational speed significantly impacts both thermal and mechanical properties that improves the FSW process by softening the hard workpiece materials. However, investigated residual stresses proves the importance of process parameters on weld quality. The results demonstrate that increasing the tool rotation speed leads to a rise in maximum temperature where for 300 rpm and 350 rpm temperature reaches 977.35 °C, 1203.6 °C respectively however for non-optimal conditions like 450 rpm this data reach to 1787 °C that may lead unsuccessful joining. Similarly, a sharp rise obtained in residual stresses on workpiece surface for 450 rpm where for 300 rpm and 350 rpm this value reach 470.76 MPa, 554.6 MPa respectively. Furthermore, higher tool rotation speeds also resulted rise in friction stress. The disparity in heat flux between the advancing side and the retreating side is attributed to the direction of tool rotation and the model accurately calculates the change in heat input on both sides.

It should be noted that the present thermo-mechanical model does not explicitly resolve the physical material flow. Therefore, flow-related defects such as voids or exit holes cannot be directly predicted. However, the model provides reliable estimates of thermal fields and residual stresses, which are known to correlate with defect formation. Future work will address this limitation by coupling the FEM framework with flow-based or ALE formulations.

No explicit failure or damage model was included in this study, as the primary aim was to evaluate thermal fields and residual stresses. Incorporation of a fracture or void nucleation model would require extensive calibration with experimental fracture tests, which is beyond the present scope but will be addressed in future work.

**Funding** The author(s) received no financial support for the research, authorship, and/or publication of this article.

**Data availability** The corresponding author declares on behalf of all authors that all raw data and materials discussed in the study will be

accessible to researcher who wants to utilise them for non-commercial research without compromising participant privacy. The corresponding author additionally provides information on where, if applicable, data might be accessed to support the findings described in the paper.

## Declarations

**Conflict of interest** The author(s) declared no potential conflicts of interest with respect to the research, authorship, and/or publication of this article.

## References


1. Mohan DG, Wu CS (2021) A review on friction stir welding of steels. Chin J Mech Eng 34(1):1–29. https://doi.org/10.1186/S10033-021-00655-3
2. Dialami N, Chiumenti M, Cervera M, Segatori A, Osikowicz W (2017) Enhanced friction model for friction stir welding (FSW) analysis: simulation and experimental validation. Int J Mech Sci 133:555–567. https://doi.org/10.1016/J.IJMECSCI.2017.09.022
3. Dewangan S, Mahajan P, Gireesh Dokala A (2022) Modelling and simulation of heat distribution and stress generation during friction stir welding of AA-6082 plates. Mater Today Proc 62:1446–1451. https://doi.org/10.1016/J.MATPR.2022.01.300
4. Sharma Y, Singh KJ, Vasudev H (2022) Experimental studies on friction stir welding of aluminium alloys. Mater Today Proc 50:2387–2391. https://doi.org/10.1016/J.MATPR.2021.10.254
5. Türkan M, Karakaş Ö (2022) Numerical modeling of defect formation in friction stir welding. Mater Today Commun 31:103539. https://doi.org/10.1016/J.MTCOMM.2022.103539
6. Tunde Azeez S, Madindwa Mashinini P (2022) Radiography examination of friction stir welds of dissimilar aluminum alloys. Mater Today Proc 62:3070–3075. https://doi.org/10.1016/J.MATPR.2022.03.225
7. Shimpi R, Sandesh Kumar C, Katarane R, Shukla AK (2022) Investigation on effects of variation of tool pin profile in a friction stir welding process by finite element approach for joining dissimilar materials. Mater Today Proc 66:1361–1364. https://doi.org/10.1016/J.MATPR.2022.05.154
8. Madhusudan M, Kumar S, Kurse S, Shanmuganatan SP, John J, Haseebuddin MR (2021) Behavioral studies of process parameters and transient numerical analysis on friction stir welded dissimilar alloys. Mater Today Proc 37(Part 2):643–647. https://doi.org/10.1016/J.MATPR.2020.05.629
9. Mugada KK, Adepu K (2019) Role of tool shoulder end features on friction stir weld characteristics of 6082 aluminum alloy. J Institution Eng (India): Ser C 100(2):343–350. https://doi.org/10.1007/S40032-018-0451-9
10. Emamian S, Awang M, Yusof F, Hussain P, Meyghani B, Zafar A (2019) The effect of pin profiles and process parameters on temperature and tensile strength in friction stir welding of AL6061 alloy. 0:15–37. Lecture Notes in Mechanical Engineering. https://doi.org/10.1007/978-981-10-9041-7_2
11. Garg A, Raturi M, Bhattacharya A (2019) Experimental and finite element analysis of progressive failure in friction stir welded AA6061-AA7075 joints. Procedia Struct Integr 17:456–463. https://doi.org/10.1016/J.PROSTR.2019.08.060
12. Abbasi M, Bagheri B, Keivani R (2015) Thermal analysis of friction stir welding process and investigation into affective parameters using simulation. J Mech Sci Technol 29(2):861–866. https://doi.org/10.1007/S12206-015-0149-3
13. Ilangovan M, Rajendra Boopathy S, Balasubramanian V (2015) Effect of tool pin profile on microstructure and tensile properties of friction stir welded dissimilar AA 6061–AA 5086 aluminium alloy joints. Def Technol 11(2):174–184. https://doi.org/10.1016/J.DT.2015.01.004
14. Chauhan P, Jain R, Pal SK, Singh SB (2018) Modeling of defects in friction stir welding using coupled Eulerian and Lagrangian method. J Manuf Process 34:158–166. https://doi.org/10.1016/J.JMAPRO.2018.05.022
15. Hynes NRJ et al (2022) Thermal behavior analysis and mechanical characterization of friction stud welded AISI 304/AA6063 joints. J Braz Soc Mech Sci Eng. https://doi.org/10.1007/S40430-022-03412-2
16. Węglowski MS (2018) Friction stir processing – state of the art. Arch Civil Mech Eng 18(1):114–129. https://doi.org/10.1016/J.ACME.2017.06.002
17. Turkan M, Karakas Ö (2021) Two different finite element models investigation of the plunge stage in joining AZ31B magnesium alloy with friction stir welding. SN Appl Sci. https://doi.org/10.1007/S42452-021-04191-6
18. Salloomi KN, Al-Sumaidae S (2021) Coupled Eulerian–Lagrangian prediction of thermal and residual stress environments in dissimilar friction stir welding of aluminum alloys. J Adv Join Processes 3:100052. https://doi.org/10.1016/J.JAJP.2021.100052
19. Al-Badour F, Merah N, Shuaib A, Bazoune A (2013) Coupled eulerian lagrangian finite element modeling of friction stir welding processes. J Mater Process Technol 213(8):1433–1439. https://doi.org/10.1016/J.JMATPROTEC.2013.02.014
20. Melaku LE, Tura AD, Mamo HB, Johnson Santhosh A, Ashok N (2022) Optimization and thermal analysis of friction stir welding on AA6061 aluminum alloys. Mater Today Proc 65:3348–3356. https://doi.org/10.1016/J.MATPR.2022.05.463
21. Kubit A, Trzepiecinski T (2020) A fully coupled thermo-mechanical numerical modelling of the refill friction stir spot welding process in alclad 7075-T6 aluminium alloy sheets. Arch Civil Mech Eng. https://doi.org/10.1007/S43452-020-00127-W
22. Cacko R, Chmielewski T, Hudycz M, Golański D (2020) New approach of friction AlN ceramics metallization with the initial FEM verification. Arch Civil Mech Eng. https://doi.org/10.1007/S43452-020-00094-2
23. Gangwar K, Ramulu M (2024) Residual stress measurement using X-ray diffraction in friction stir-welded dissimilar titanium alloys. Materials. https://doi.org/10.3390/ma17071482
24. Wang B, Zhu P, Cao Y, Zhou L, Xue P, Wu L (2023) Effects of different friction stir welding processes on residual stress and deformation of Ti62A alloy joints. J Mater Res Technol 26:6096–6107. https://doi.org/10.1016/j.jmrt.2023.08.308
25. Yoshikawa G, Miyasaka F, Hirata Y, Katayama Y, Fuse T (2012) Development of numerical simulation model for FSW employing particle method. Sci Technol Weld Joining 17(4):225–263. https://doi.org/10.1179/1362171811Y.0000000099
26. Tartakovsky A, Grant G, Sun X, Khaleel M (2006) Modeling of friction stir welding (FSW) process with smooth particle hydrodynamics (SPH). SAE Technical Paper 2006-01-1394. https://doi.org/10.4271/2006-01-1394
27. Quintana KJ, Silveira JLL (2018) Analysis for the forces in FSW for aluminum alloy considering tool geometry and process velocities. J Braz Soc Mech Sci Eng. https://doi.org/10.1007/s40430-018-1162-0
28. Zhu XK, Chao YJ (2004) Numerical simulation of transient temperature and residual stresses in friction stir welding of 304L stainless steel. J Mater Process Technol 146(2):263–272. https://doi.org/10.1016/J.JMATPROTEC.2003.10.025
29. Granta ANSYS Material Properties
30. Assidi M, Fourment L, Guerdoux S, Nelson T (2010) Friction model for friction stir welding process simulation: calibrations from welding experiments. Int J Mach Tools Manuf 50(2):143–155. https://doi.org/10.1016/J.IJMACHTOOLS.2009.11.008

31. Riahi M, Nazari H (2011) Analysis of transient temperature and residual thermal stresses in friction stir welding of aluminum alloy 6061-T6 via numerical simulation. Int J Adv Manuf Technol 55(1–4):143–152. https://doi.org/10.1007/S00170-010-3038-Z
32. Sarikavak Y (2021) An advanced modelling to improve the prediction of thermal distribution in friction stir welding (FSW) for difficult to weld materials. J Brazilian Soc Mech Sci Eng 43(1):1–14. https://doi.org/10.1007/s40430-020-02735-2
33. Wu T, Zhao F, Luo H, Wang H, Li Y (2019) Temperature monitoring and material flow characteristics of friction stir welded 2A14-t6 aerospace aluminum alloy. Materials. https://doi.org/10.3390/ma12203387
34. Sugiarto MS, Ma'Arif H, Purwanto WJE, Mahendra H, Oswari (2023) CHARACTERISTIC OF FRICTION STIR WELDING WELD JOINT OF AA 6061 ON INITIAL TEMPERATURE DIFFERENCE. MM Sci J 2023–March:6385–6392. https://doi.org/10.17973/MMSJ.2023_03_2022094
35. Technology Showcase Example Problems, 2023. [Online]. Available: http://www.ansys.com
36. Metallic Materials Properties (2022) Development and standardization (MMPDS-17), chap. Battelle Memorial Institute, pp 1–9
37. Veljic DM, Rakin M, Radakovic Z, Todorovic PM (2013) Heat generation during plunge stage in friction stir welding. Therm Sci. https://doi.org/10.2298/TSCI120301205V
38. Zhang Z (2008) Comparison of two contact models in the simulation of friction stir welding process. J Mater Sci 43:5867–5877. https://doi.org/10.1007/s10853-008-2865-x
39. Feng Z, Wang XL, David SA, Sklad PS (2007) Modelling of residual stresses and property distributions in friction stir welds of aluminium alloy 6061-T6. Sci Technol Weld Joining 12(4):348–356. https://doi.org/10.1179/174329307X197610
40. Aziz SB, Dewan MW, Huggett DJ, Wahab MA, Okeil AM, Liao TW (2017) A fully coupled thermomechanical model of friction stir welding (FSW) and numerical studies on process parameters of lightweight aluminum alloy. Acta Metall Sinica (English Letters) No Oct. https://doi.org/10.1007/s40195-017-0658-4
41. Zubelewicz A (2019) Century-long Taylor-Quinney interpretation of plasticity-induced heating reexamined. Sci Rep. https://doi.org/10.1038/s41598-019-45533-0
42. Liu Q et al (2022) Temperature-dependent friction coefficient and its effect on modeling friction stir welding for aluminum alloys. J Manuf Process 84:1054–1063. https://doi.org/10.1016/J.JMAPRO.2022.10.068
43. Veljić DM et al (2013) Heat generation during plunge stage in friction stir welding. Therm Sci 17(2):489–496. https://doi.org/10.2298/TSCI120301205V
44. Soundararajan V, Zekovic S, Kovacevic R (2005) Thermo-mechanical model with adaptive boundary conditions for friction stir welding of al 6061. Int J Mach Tools Manuf 45:1577–1587. https://doi.org/10.1016/j.ijmachtools.2005.02.008
45. Bhowmik A, Kumar Dewangan S, Nandan Banjare P, Kumar Manoj M (2023) Material flow behavior and mechanical characterization of dissimilar friction stir welded Cu-Mg alloy joints. Mater Today Proc. https://doi.org/10.1016/j.matpr.2023.06.056
46. Zhu XK, Chao YJ (2002) Effects of temperature-dependent material properties on welding simulation. Comput Struct 80(11):967–976. https://doi.org/10.1016/S0045-7949(02)00040-8
47. Pankaj P, Tiwari A, Dhara LN, Raj S, Biswas P (2022) Investigations on the effect of sheets positioning in advancing & retreating side for dissimilar FSW of DH36 steel and aluminum alloy 6061. J Institution Eng (India): Ser C 103(1):5–20. https://doi.org/10.1007/s40032-021-00714-7
48. Sahu PK, Kumari K, Pal S, Pal SK (2016) Hybrid fuzzy-grey-Taguchi based multi weld quality optimization of Al/Cu dissimilar friction stir welded joints. Adv Manuf 4(3):237–247. https://doi.org/10.1007/s40436-016-0151-8
49. Salih OS, Ou H, Sun W (2023) Heat generation, plastic deformation and residual stresses in friction stir welding of aluminium alloy. Int J Mech Sci. https://doi.org/10.1016/J.IJMECSCI.2022.107827


**Publisher's Note** Springer Nature remains neutral with regard to jurisdictional claims in published maps and institutional affiliations.

Springer Nature or its licensor (e.g. a society or other partner) holds exclusive rights to this article under a publishing agreement with the author(s) or other rightsholder(s); author self-archiving of the accepted manuscript version of this article is solely governed by the terms of such publishing agreement and applicable law.